# Chapter 3

# Flow Field

The measurements of the flow field in the wind tunnel working section described in this chapter were made without the cylinder model installed.

## 3.1 End Plate Positions

Large end plates anchored to the walls of the wind tunnel were used to ensure as great a degree of uniformity of the cylinder wake flow as possible. Their function was to reduce the depth of the wall boundary layer at the model position by starting a new boundary layer outside that developed on the main wall of the tunnel. The dimensions of the end plates were given in chapter 2, figure 2.2.

Given the width of working section and tunnel blockage ratio, the distance between the end plates and working section walls is a compromise between wall boundary layer depth and cylinder aspect ratio. The thickness of the wall boundary layers was established in smooth flow at an air speed in the middle of the working range, using a Pitot rake and inclined manometer bank. The end plates were then placed 45 mm away from the main tunnel walls. Wall boundary layer profiles before and after the fitting of end plates are shown in figure 3.1.

## 3.2 Static Pressure Distribution

The longitudinal distribution of static pressure on the roof of the working section is shown in figure 3.2. The pressure coefficient was computed using the static and dynamic pressures from a Pitot-static tube located four cylinder diameters upstream of the model position. Static pressure tapping tubes with ends flush to the walls of the tunnel were used for the measurements, which were taken using a Betz water manometer.

The main point of the measurements was to verify that leakage of air into the working section from the surroundings was minimal, since the working section operated slightly below atmospheric pressure; the largest drop recorded was 150 mm water head. It was found that the variation in static pressure was measurably reduced by sealing gaps between the various particle board panels which made up the working section walls. The

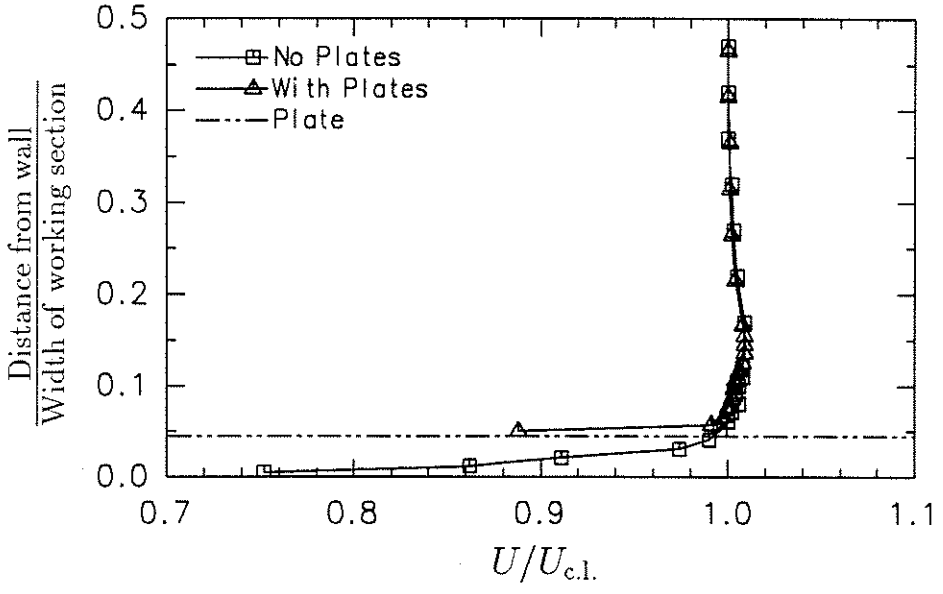


FIGURE 3.1: Boundary layer mean velocity profiles measured near the wall of the working section, with and without end plates in position.

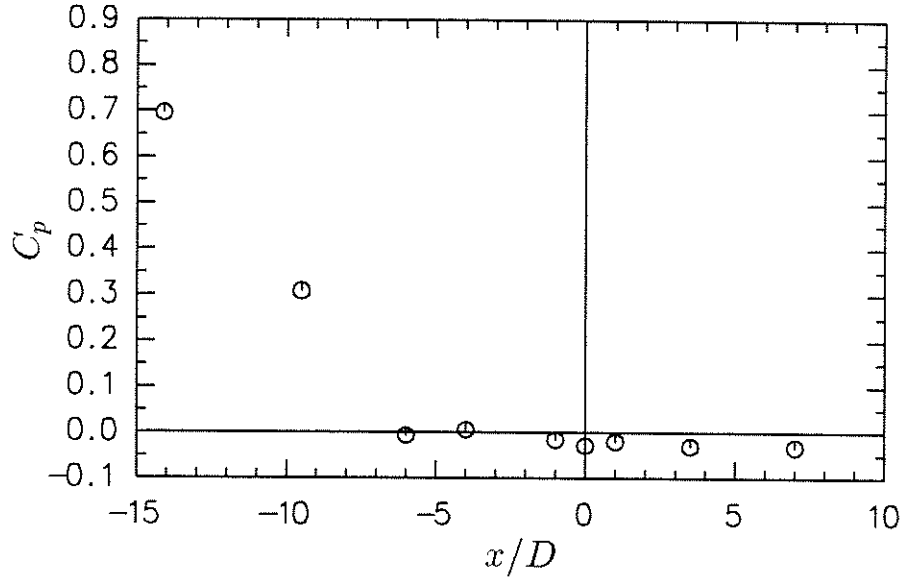


FIGURE 3.2: Working section roof static pressure profile

measurements show that the final static pressure variation in the streamwise direction was small, and unlikely to have any measurable effect on the experimental results; hence no attempt was made to achieve further reduction.

## 3.3 Anemometry

The data in the following sections were measured using the hotwire equipment described in chapter 2. This section describes a procedure devised to compensate anemometer output for slow increases in temperature, caused by viscous effects, which occurred in

the closed circuit wind tunnel during measurements. These changes alter the calibration of the anemometer if not accounted for.

The new method is a generalization of those presented by Bearman (1969 b) and Jancauskas (1983). The accuracy of temperature compensation of mean velocities provided by the new method was similar to Bearman's, but with the practical advantage that the form of the linearizing function does not need to be known in advance. (Bearman's method related only to the linearization function of the University of Southampton linearized hotwire anemometer.) Since the technique differs from the others mainly in the way in which the performance characteristics of the anemometer circuitry is described, only a brief outline will be given here.

All three methods rely on calibrations obtained for both the linearized and unlinearized anemometer bridge outputs. These calibrations relate voltage outputs to mean velocities measured in smooth flow; some other device, such as a Pitot-static tube, serves as a velocity reference. The new method used a seventh-order—odd terms only—polynomial relationship fitted between the two sets of voltages, and since the input to the linearizer unit is the unlinearized bridge output, this describes the linearizer function. Heat transfer theory was used to relate unlinearized bridge outputs made at one air temperature to those at the reference temperature, as described by Bearman. (The reference temperature is the one at which the linearizer output was adjusted to zero voltage in the absence of flow.) Another seventh-order polynomial was used to relate mean velocities to unlinearized bridge output voltages corrected to the reference temperature.

Temperature compensation for mean velocity then proceeded as follows:

1. Linearizer voltage was converted to an equivalent unlinearized bridge voltage using the fitted relationship.

2. The equivalent bridge voltage was related to one at the reference temperature, using heat transfer theory and a measurement of the air temperature at which the linearized voltage was recorded.

3. This temperature compensated bridge voltage was used to estimate the mean airspeed at the probe.

An extension of the method, which used the derivatives of the fitted polynomials, provided temperature compensation of the fluctuating linearizer voltages.

A simpler method would have been to work with the unlinearized bridge output directly, and so avoid the additional complication of modelling the analogue linearizer circuit. This presents theoretical problems in highly turbulent flows; due to the highly nonlinear bridge characteristic it becomes difficult to reliably relate fluctuating voltages to velocities. A less obvious practical problem is that small quantization increments are required of the analogue-to-digital converter used, particularly when measuring low turbulence intensity flows. The cause of the problem is the shape of the relationship between velocity and unlinearized bridge voltage, which becomes flat at high velocities. This means that comparatively large velocity fluctuations are needed to span more than a few voltage quantization levels in low turbulence intensity flows. As a result, measurements of turbulence statistics would become swamped by quantization noise

unless a high resolution analogue-to-digital converter is used. By working with the linearized bridge output, the sensitivity of voltage to velocity fluctuations remained essentially the same for all velocities, and the resolution problem was much less severe.

## 3.4 Mean Velocity Profiles

Taken overall, the profiles indicate that the spanwise uniformity of mean velocity was good, typically within 2% of the tunnel centreline airspeed. An exception was the profile achieved with the 100 mm slat grid, where the maximum deviation recorded was 8% of the tunnel centreline value (5% of the average value). A vertical velocity profile recorded in smooth flow indicates that the flow was reasonably uniform in the cross flow direction, as figure 3.4 shows. The maximum deviation of 7% from the model centreline velocity was measured at the tunnel roof, five cylinder diameters from the centreline.

### 3.4.1 Smooth Flow

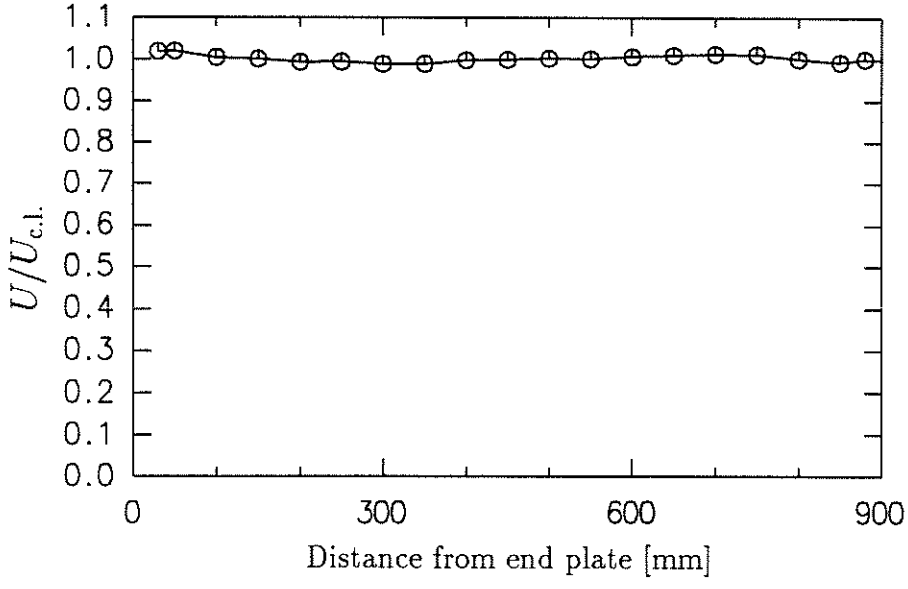


FIGURE 3.3: Spanwise distribution of mean velocity in smooth flow, measured at model position.

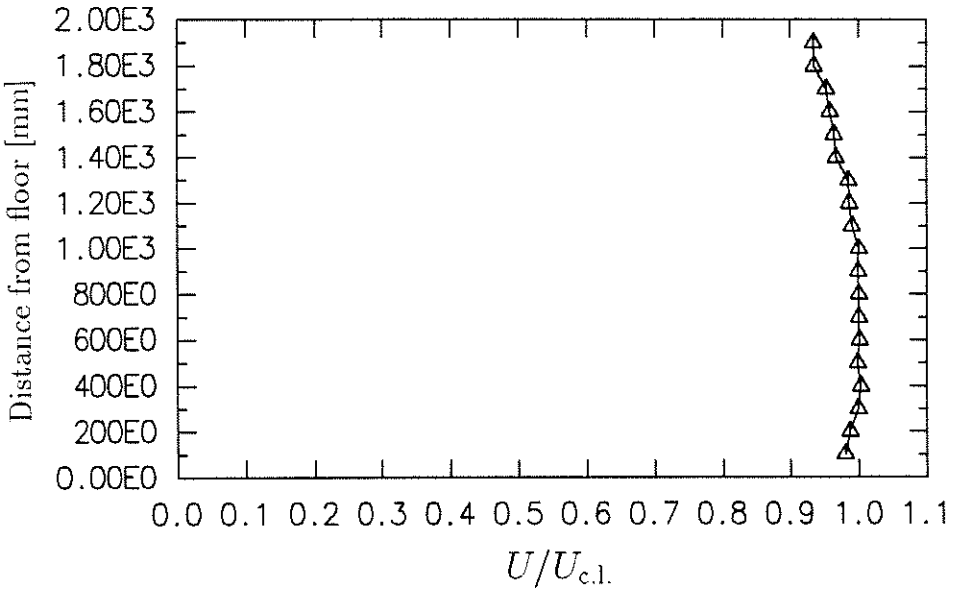


FIGURE 3.4: Vertical distribution of mean velocity in smooth flow, measured on tunnel centreline at model position.

### 3.4.2 300 mm Slat Grid, Position "A"

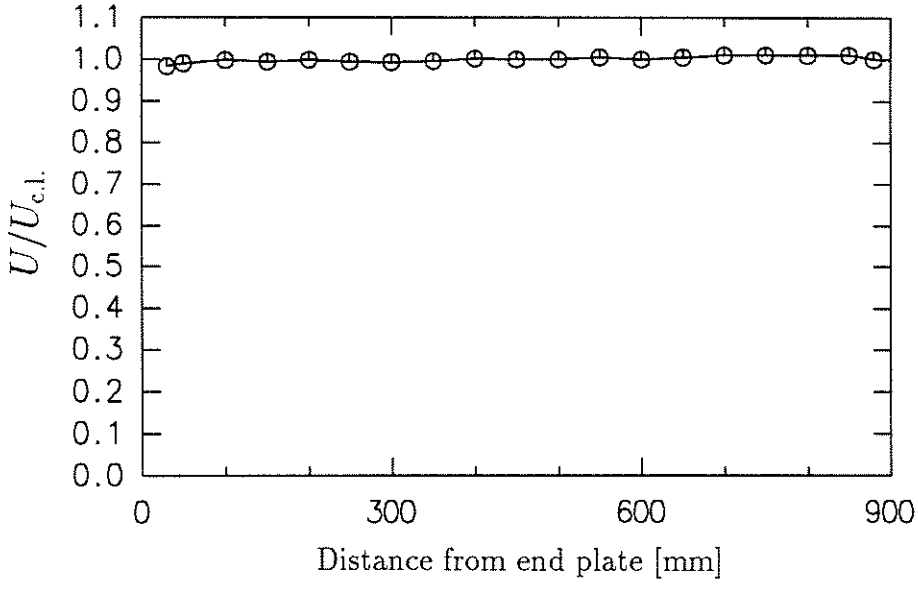


FIGURE 3.5: Spanwise distribution of mean velocity with 300 mm slat grid, position "A".

### 3.4.3 300 mm Slat Grid, Position "B"

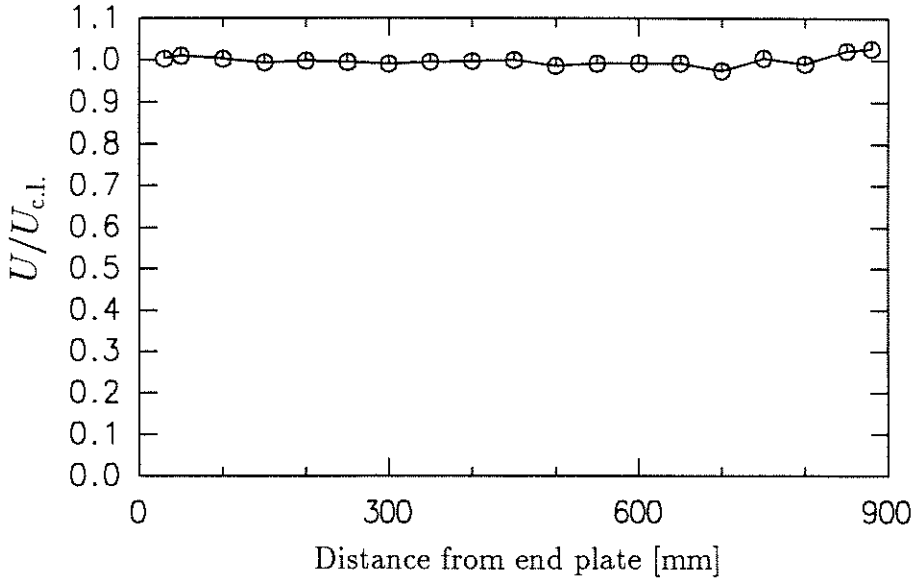


FIGURE 3.6: Spanwise distribution of mean velocity with 300 mm slat grid, position "B".

### 3.4.4 300 mm Slat Grid, Position "C"

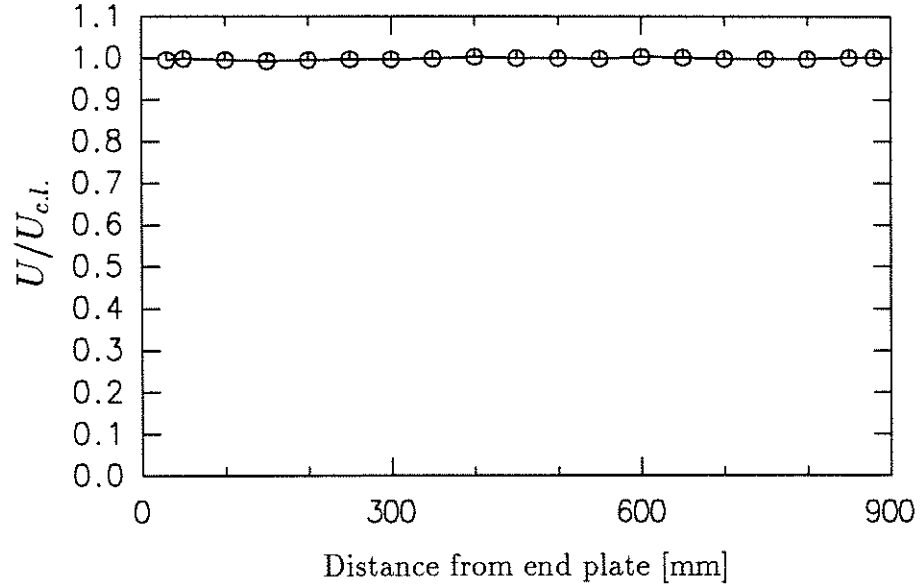


FIGURE 3.7: Spanwise distribution of mean velocity with 300 mm slat grid, position "C".

### 3.4.5 100 mm Slat Grid, Position "B"

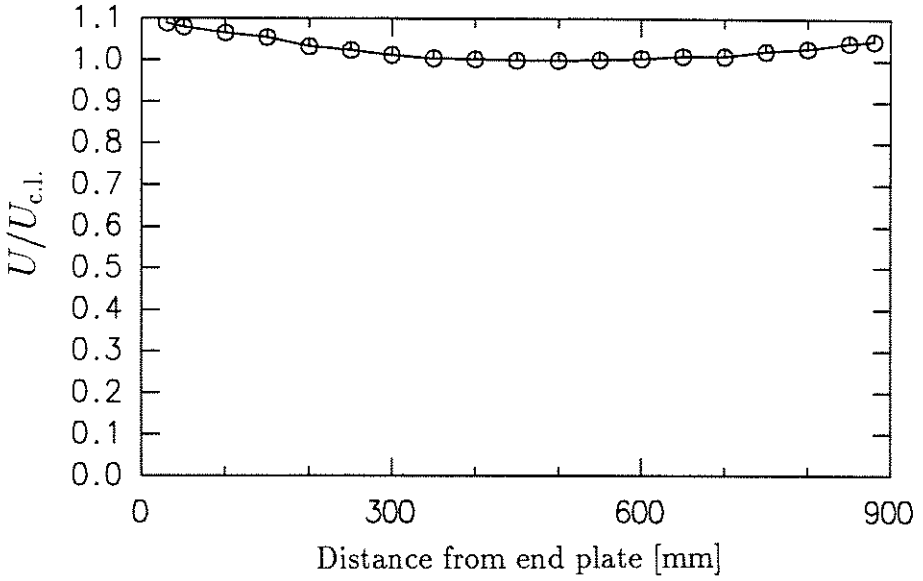


FIGURE 3.8: Spanwise distribution of mean velocity with 100 mm slat grid, position "B".

## 3.5 Turbulence Intensity Profiles

Measurements of spanwise distribution of turbulence intensity were made using crossed sensor hotfilm probes, so the longitudinal and cross flow turbulence intensities could be measured. The crossed sensor probe was oriented such that the planes in which the sensors lay were parallel with the vertical walls of the working section. As a check, the longitudinal intensities were also measured using a single sensor probe; the longitudinal measurements taken using the two different types of probes were in agreement and the values presented are the average of the two sets.

Figure 3.9 shows the spanwise distributions of longitudinal turbulence intensity $I_u = \sigma_u/U$, where $\sigma_u$ is the standard deviation of the fluctuating streamwise velocity and $U$ is the mean velocity.

Figure 3.10 shows the spanwise distributions of cross flow turbulence intensity $I_v = \sigma_v/U$, where $\sigma_v$ is the standard deviation of the fluctuating cross flow velocity.

A comparison of the distributions of $I_u$ and $I_v$ indicates that the turbulence was not isotropic for the cases of the 300 mm grid at positions "A" and "B", since the longitudinal and cross flow intensities were unequal. Further, the lack of spanwise uniformity of the distributions for the 300 mm grid in position "A" indicates that localized effects from the grid were still in evidence at the model position. These deviations from isotropy were considered to be an unavoidable side-effect of large turbulence intensities and scales in grid turbulence and the result represents a compromise between the two conflicting sets of requirements.

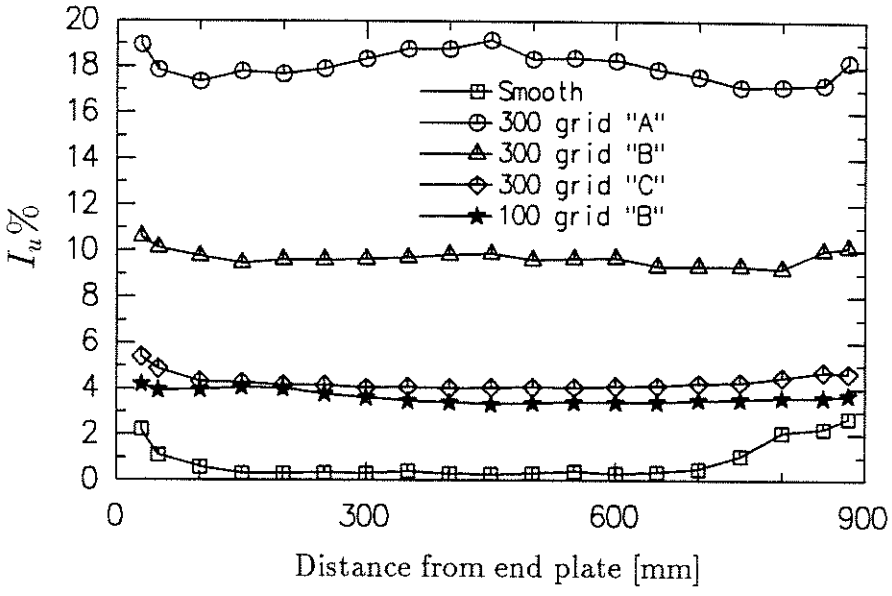


FIGURE 3.9: Spanwise distribution of longitudinal turbulence intensities, $I_u$

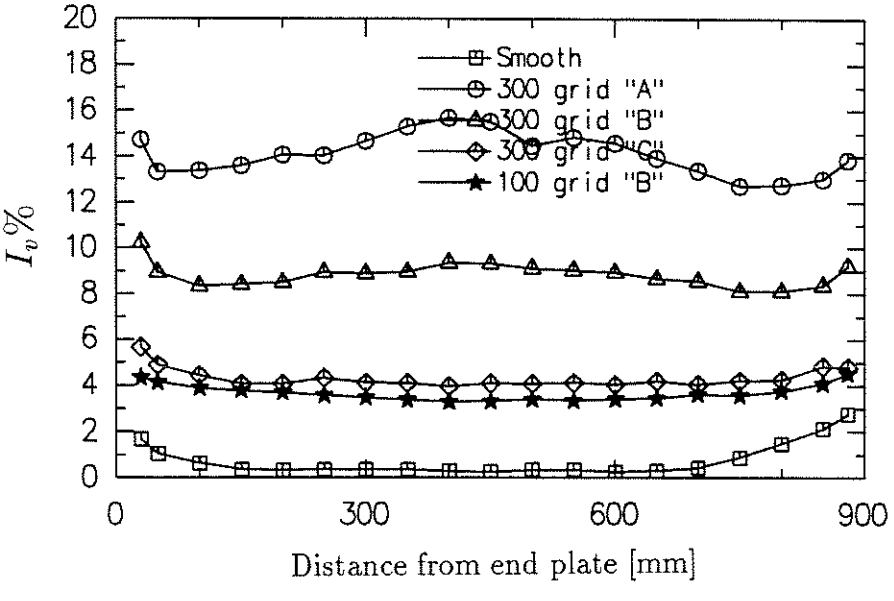


FIGURE 3.10: Spanwise distribution of cross flow turbulence intensities, $I_v$

## 3.6 Turbulence Spectra and Length Scales

For computation of turbulence spectra and length scales, linearized anemometer outputs were low-pass filtered and sampled. Autospectra of the longitudinal velocity fluctuations were then computed from the recorded time series and plotted. To evaluate integral longitudinal turbulence length scales, von Kármán turbulence spectra were fitted "by eye" to the plotted spectra after they had been suitably normalized. Kármán spectra can be written in the form

$$\frac{\Upsilon S_u(\Upsilon)}{\sigma_u^2} = \frac{4\Upsilon L_u^x}{\left[1 + 70.8\,(\Upsilon L_u^x)^2\right]^{5/6}}\,. \tag{3.1}$$

Here, $\Upsilon$ is the inverse wavelength of turbulence, or $f/U$ under Taylor's hypothesis, where $f$ is frequency and $U$ is the mean longitudinal velocity, $\sigma_u^2$ is the variance of the longitudinal velocity fluctuations, and $L_u^x$ is a longitudinal integral scale for the turbulence.

The resulting measured and fitted spectra are shown in the following plots. In most cases, there is good correspondence between the shapes of the measured and fitted spectra. For the "smooth" flow the fitted spectrum does not match the shape of the measured spectrum since there was little inertial sub-range, the shape of the measured spectrum indicating rapid progression from generation to dissipation scales.

### 3.6.1 Smooth Flow

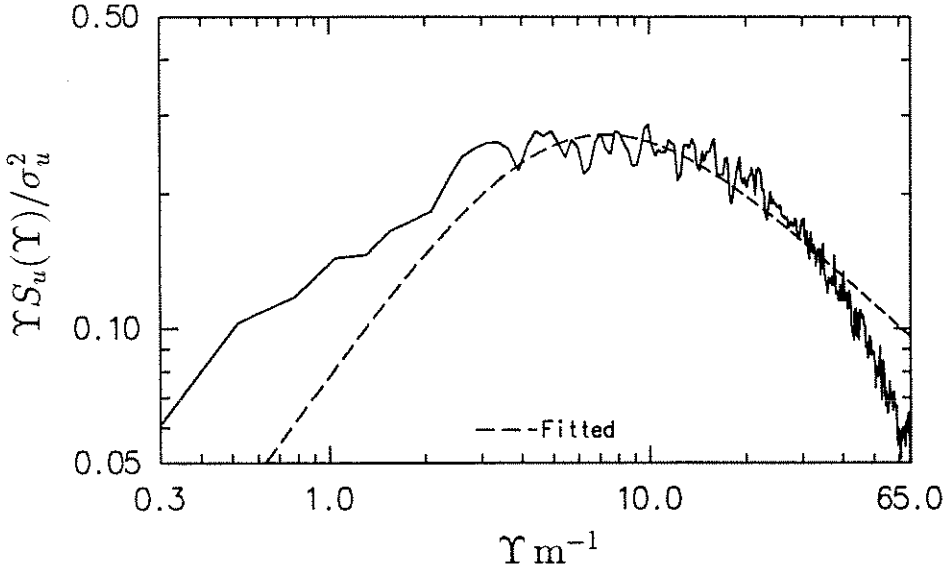


FIGURE 3.11: Longitudinal turbulence spectrum in smooth flow. Fitted integral scale $L_u^x = 0.020\,\mathrm{m}$.

### 3.6.2 300 mm Slat Grid, Position "A"

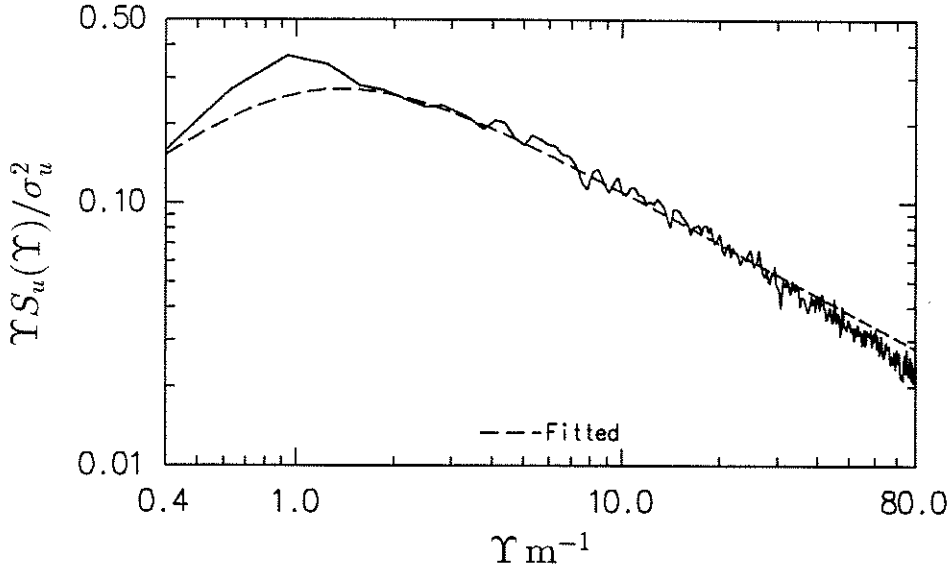


FIGURE 3.12: Longitudinal turbulence spectrum with 300 mm slat grid, position "A". Fitted integral scale $L_u^x = 0.105\,\mathrm{m}$.

### 3.6.3 300 mm Slat Grid, Position "B"

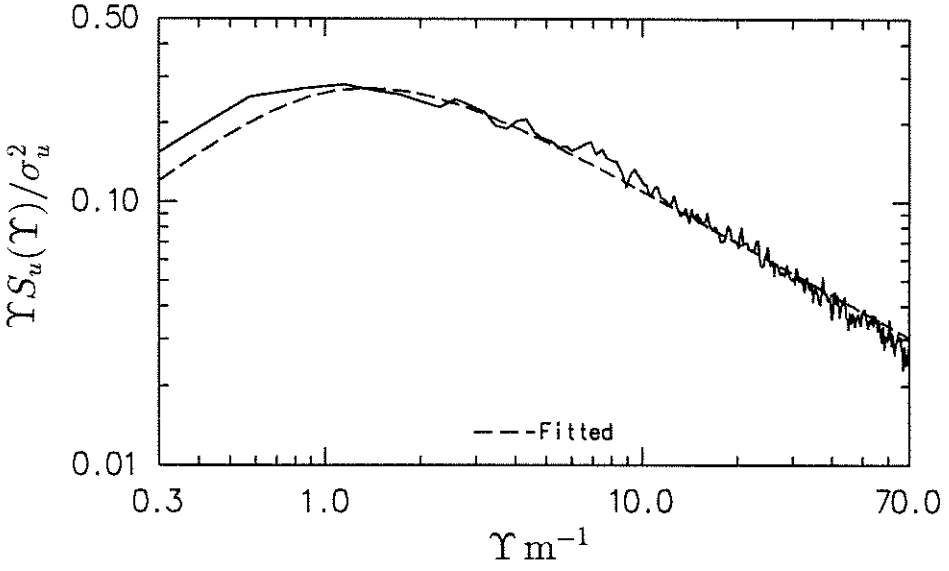


FIGURE 3.13: Longitudinal turbulence spectrum with 300 mm slat grid, position "B". Fitted integral scale $L_u^x = 0.105\,\mathrm{m}$.

### 3.6.4 300 mm Slat Grid, Position "C"

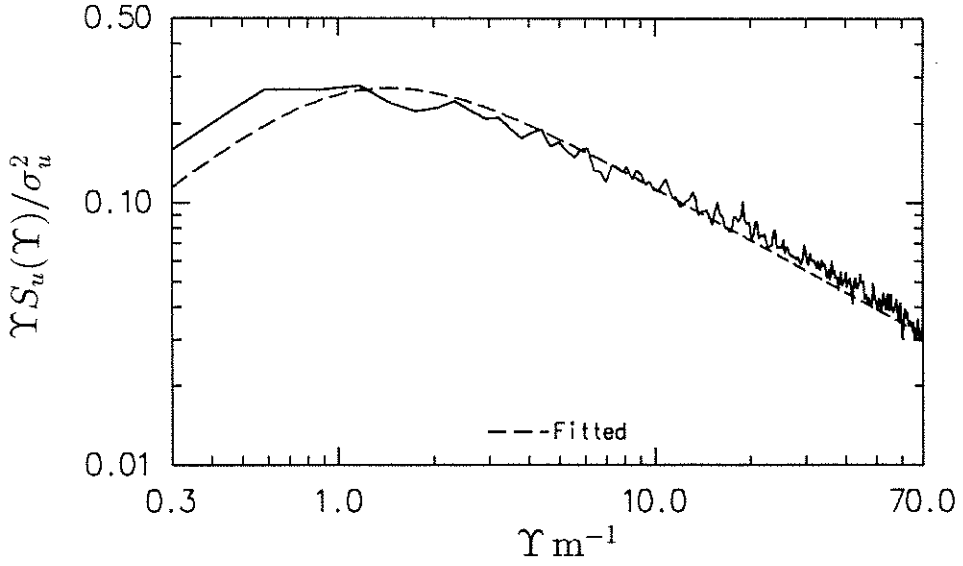


FIGURE 3.14: Longitudinal turbulence spectrum with 300 mm slat grid, position "C". Fitted integral scale $L_u^x = 0.100\,\mathrm{m}$.

### 3.6.5 100 mm Slat Grid, Position "B"

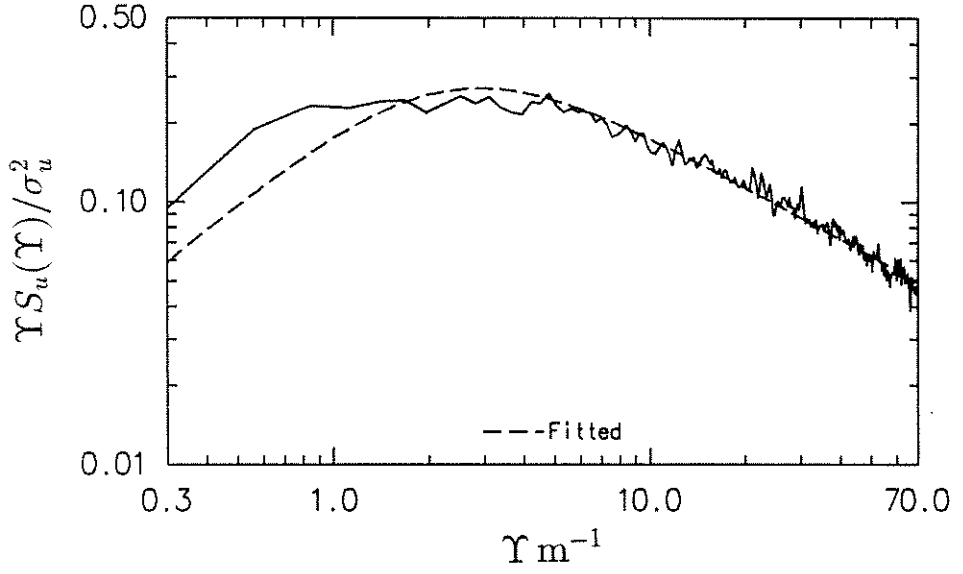


FIGURE 3.15: Longitudinal turbulence spectrum with 100 mm slat grid, position "B". Fitted integral scale $L_u^x = 0.050\,\mathrm{m}$.

## 3.7 Summary

The spanwise averages of the longitudinal and transverse turbulence intensities together with the integral length scales are presented in table 3.1. For ease of reference, the turbulent flow configurations are given numbers which will be in the remainder of this thesis.

TABLE 3.1: Spanwise averaged turbulence intensities for the five flow configurations

| Configuration | Description | $I_u$% | $I_v$% | LSR |
|---|---|---|---|---|
| "Smooth Flow" | Screens & Honeycomb | 0.6 | 0.6 | 0.10 |
| 1 | 100 mm Grid, Position "B" | 3.6 | 3.6 | 0.25 |
| 2 | 300 mm Grid, Position "C" | 4.2 | 4.2 | 0.50 |
| 3 | 300 mm Grid, Position "B" | 9.6 | 8.7 | 0.53 |
| 4 | 300 mm Grid, Position "A" | 18.0 | 14.1 | 0.53 |

It is apparent that the 100 mm grid (Config. 1) provided an integral scale about half that of the other grids, but gave a similar turbulence intensity as the 300 mm grid in position "C" (Config. 2). This allows an assessment of sensitivity of lift forces to turbulence scale to be made in this case.

The turbulence became less isotropic as intensity increased, on the evidence that the intensities $I_u$ and $I_v$ diverged. This reduction in isotropy is thought to be unavoidable in grid-generated turbulence of these large intensities and scales. It is difficult to gauge the practical importance of the anisotropy shown, since full-size flows with large turbulence intensities are unlikely to be isotropic.